JCB Journal of Cell Biology

ARTICLE

Nucleoplasmin is a limiting component in the scaling of nuclear size with cytoplasmic volume

Pan Chen[1], Miroslav Tomschik[1], Katherine M. Nelson[1,2], John Oakey[2], Jesse C. Gatlin[1], and Daniel L. Levy[1]

How nuclear size is regulated relative to cell size is a fundamental cell biological question. Reductions in both cell and nuclear sizes during *Xenopus laevis* embryogenesis provide a robust scaling system to study mechanisms of nuclear size regulation. To test if the volume of embryonic cytoplasm is limiting for nuclear growth, we encapsulated gastrula-stage embryonic cytoplasm and nuclei in droplets of defined volume using microfluidics. Nuclei grew and reached new steady-state sizes as a function of cytoplasmic volume, supporting a limiting component mechanism of nuclear size control. Through biochemical fractionation, we identified the histone chaperone nucleoplasmin (Npm2) as a putative nuclear size effector. Cellular amounts of Npm2 decrease over development, and nuclear size was sensitive to Npm2 levels both in vitro and in vivo, affecting nuclear histone levels and chromatin organization. We propose that reductions in cell volume and the amounts of limiting components, such as Npm2, contribute to developmental nuclear size scaling.

Introduction

A fundamental question in cell biology is how organelle sizes are regulated. Nuclear size control is of particular interest, as there are dramatic reductions in nuclear size during early development (Hara et al., 2013; Jevtić and Levy, 2015) and nuclear size tends to scale with cell size in different species and cell types (Conklin, 1912; Wilson, 1925). Furthermore, increased nuclear size is almost uniformly used for cancer diagnosis and prognosis (Jevtić and Levy, 2014; Zink et al., 2004). Nuclear size may therefore play important roles in normal development and cell physiology as well as disease. Elucidating the functional significance of nuclear size in these various settings requires a mechanistic understanding of the factors and pathways that impinge on the size of the nucleus.

Size control of intracellular structures can be effectively studied in early *Xenopus laevis* embryos. After fertilization, the large 1.2-mm single cell divides rapidly 12 times without cell growth, giving rise to ~4,000 much smaller cells spanning developmental stages 1–8 (Nieuwkoop and Faber, 1967). Stage 8 coincides with the midblastula transition (MBT), characterized by marked slowing of cell cycles and up-regulation of zygotic transcription (Newport and Kirschner, 1982). Gastrulation ensues, encompassing stages 10–12. Between stages 4 and 8 (i.e., pre-MBT), average cell volume decreases ~160-fold with a concomitant 3.7-fold reduction in nuclear volume; from stages 8 to 12 (i.e., post-MBT), a more modest 8-fold reduction in cell volume is accompanied by a 3.4-fold reduction in nuclear volume (Jevtić and Levy, 2015). This reproducible scaling of nuclear size provides a robust system with which to characterize and identify mechanisms of nuclear size regulation.

Two non-mutually exclusive models might be invoked to explain how nuclear size scales over development: (1) the expression or localization of developmental regulators of nuclear size may change as development proceeds, and/or (2) the maternal protein pool in the egg contains nuclear assembly or growth components that become limiting as they are partitioned into smaller and smaller cells over development (Goehring and Hyman, 2012). One developmental regulator of *X. laevis* nuclear size scaling is nucleocytoplasmic transport. In pre-MBT *X. laevis* embryos, cytoplasmic levels of importin α decrease due to membrane partitioning, leading to reduced nuclear import kinetics and contributing to early developmental reductions in nuclear size (Brownlee and Heald, 2019; Levy and Heald, 2010; Wilbur and Heald, 2013). Importin α cargos important for nuclear growth are nuclear lamins (Newport et al., 1990), intermediate filament proteins that incorporate into the nuclear lamina that underlines the inner nuclear membrane. In post-MBT *X. laevis* embryos, redistribution of a population of PKC from the cytoplasm to the nucleus leads to phosphorylation-dependent changes in the association of lamins with the nuclear envelope (NE) and concomitant reductions in nuclear size (Edens et al., 2017; Edens and Levy, 2014). Thus, changes in the expression and/or localization of

---

[1]Department of Molecular Biology, University of Wyoming, Laramie, WY; [2]Department of Chemical Engineering, University of Wyoming, Laramie, WY.

Correspondence to Daniel L. Levy: dlevy1@uwyo.edu.

importin α, lamins, and PKC all contribute to developmental nuclear size scaling in *X. laevis*.

Less studied is whether limiting components might regulate nuclear size. Microinjection of nuclei into *X. laevis* oocytes resulted in nuclear growth with clustered nuclei growing less (Gurdon, 1976), similar to what has been observed in multinucleate fission yeast cells (Neumann and Nurse, 2007). Consistent with the idea that the amount of surrounding cytoplasm might limit nuclear growth, nuclei assembled in *X. laevis* egg extract grew less when confined in narrow microfluidic channels as opposed to wider channels. Furthermore, the extent of nuclear growth correlated with the available cytoplasmic space in which interphase microtubule asters could grow, supporting a microtubule-based mechanism for how spatial constraints might limit nuclear growth and steady-state size (Hara and Merten, 2015). Here, we test if the volume of embryonic cytoplasm is limiting for nuclear growth, focusing on post-MBT nuclear size scaling, and use biochemical fractionation to identify putative limiting components.

Results

Cytoplasmic volume contributes to nuclear size scaling in *X. laevis* embryo extracts

During normal *X. laevis* embryogenesis, individual nuclear volumes scale smaller between the MBT and early gastrulation (stages 8–10.5; Fig. 1 A). Because cell sizes also become smaller during this time period, we wondered if cytoplasmic volume might contribute to observed nuclear size scaling. To test this hypothesis, we isolated extract containing embryonic cytoplasm and endogenous embryonic nuclei from stage 10 to 10.5 embryos, which have average blastomere volumes of 0.07 nl and steady-state nuclear sizes (Fig. S1 A). We then used microfluidic droplet-generating devices to encapsulate this extract in droplets of different volumes and shapes and visualized nuclei by uptake of GFP–NLS (Fig. 1 A). Unless otherwise noted, we only analyzed droplets containing one nucleus. After an incubation period, we observed that nuclei grew larger in ∼0.8-nl spherical droplets compared with ∼0.1-nl spherical droplets (Fig. 1 B and Video 1), while droplet volume did not change over time (Fig. S1 B). Nuclei generally reached a new steady-state size after 3–4 h, consistent with an average cell cycle length of ∼4 h at this stage of development (Duncan and Su, 2004; Murakami et al., 2004). Nuclear volume increased 3.2-fold in ∼0.8-nl spherical droplets but only 1.9-fold in ∼0.1-nl spherical droplets (Fig. 1 C). In addition, the nuclear growth speed was faster in large droplets than small droplets (Fig. S1 C), consistent with limiting components being more rapidly depleted in small droplets. Furthermore, in droplets containing multiple nuclei, the growth of individual nuclei was reduced compared with nuclear growth in similarly sized droplets containing one nucleus (Fig. S1 D). These data indicate that the available volume of embryonic cytoplasm can limit nuclear growth.

Because cell dimensions decrease over development in addition to cell volume, we next investigated if nuclear size might be sensitive to cell shape. To test this idea, we generated flattened droplets with a greatly reduced width in one dimension (Fig. 1 A). Nuclei still grew in flattened droplets and to a similar extent as in spheres with comparable volumes (Fig. 1, D and E; and Fig. S1 E), indicating that in this system cytoplasmic volume, not shape, scales nuclear size. To test if microtubules contribute to nuclear size scaling in post-MBT embryonic extracts, we encapsulated stage 10 embryo extract treated with nocodazole. In the absence of microtubules, encapsulated nuclei still grew and to a similar extent as in similarly sized droplets containing microtubules (Fig. S1 F), and microtubule depolymerization did not reduce the size of stage 10 nuclei in vivo (Fig. S1 G). Taken together, these results demonstrate that nuclear growth and steady-state size scale with cytoplasmic volume in *X. laevis* embryo extracts, independently of cytoplasmic shape and microtubules.

Cytoplasmic composition contributes to nuclear size scaling in post-MBT *X. laevis* embryos

We noted that in droplets greater than ∼0.5 nl, the increase in nuclear volume reached a plateau of 3- to 3.5-fold (Fig. 1 E). To place this in an in vivo context, we compared nuclear sizes at different developmental stages to our in vitro encapsulation data. When stage 10 extract and nuclei were encapsulated in droplets having similar volumes as cells in stage 8 and 9 embryos, although nuclei grew significantly, they did not reach stage 8 and 9 in vivo nuclear sizes (Fig. 2 A). These data suggest that cytoplasmic volume is not sufficient to account for post-MBT nuclear size scaling. To investigate if changes in cytoplasmic composition might contribute to nuclear size scaling, we isolated stage 10 nuclei and resuspended them in cytoplasm from earlier embryonic stages. Nuclei in stage 5 cytoplasm grew more than nuclei in stage 6.5 cytoplasm that in turn grew more than nuclei in stage 10 cytoplasm (Fig. 2, B and C). These data indicate that differences in the cytoplasmic composition of earlier stage embryos may contribute to nuclear size scaling in *X. laevis* embryo extracts. Additionally, because nucleus number increases as development proceeds, components limiting for nuclear growth may become increasingly sequestered into growing numbers of nuclei and concomitantly depleted from the cytoplasm. For this reason, the cytoplasmic concentration of limiting components could be higher in earlier stage extracts. Thus, a limiting component model may explain how both volume and stage-dependent differences in cytoplasmic composition contribute to nuclear size scaling.

Npm2 is a nuclear size effector

Because our data suggested that one or more cytoplasmic components are limiting for nuclear growth, we undertook a biochemical fractionation approach to identify putative limiting components. We reasoned that *X. laevis* egg extract would be a good starting material rather than stage 10 embryo extract, because (1) fractionation necessitates large extract volumes and it is straightforward to obtain sufficiently large volumes of egg extract, but not embryo extract; (2) egg extract contains large amounts of stockpiled maternal proteins; and (3) unencapsulated egg extract induces significant growth of stage 10 nuclei (Fig. 2 D), providing a relatively facile assay for nuclear sizing activities without time-consuming microfluidic

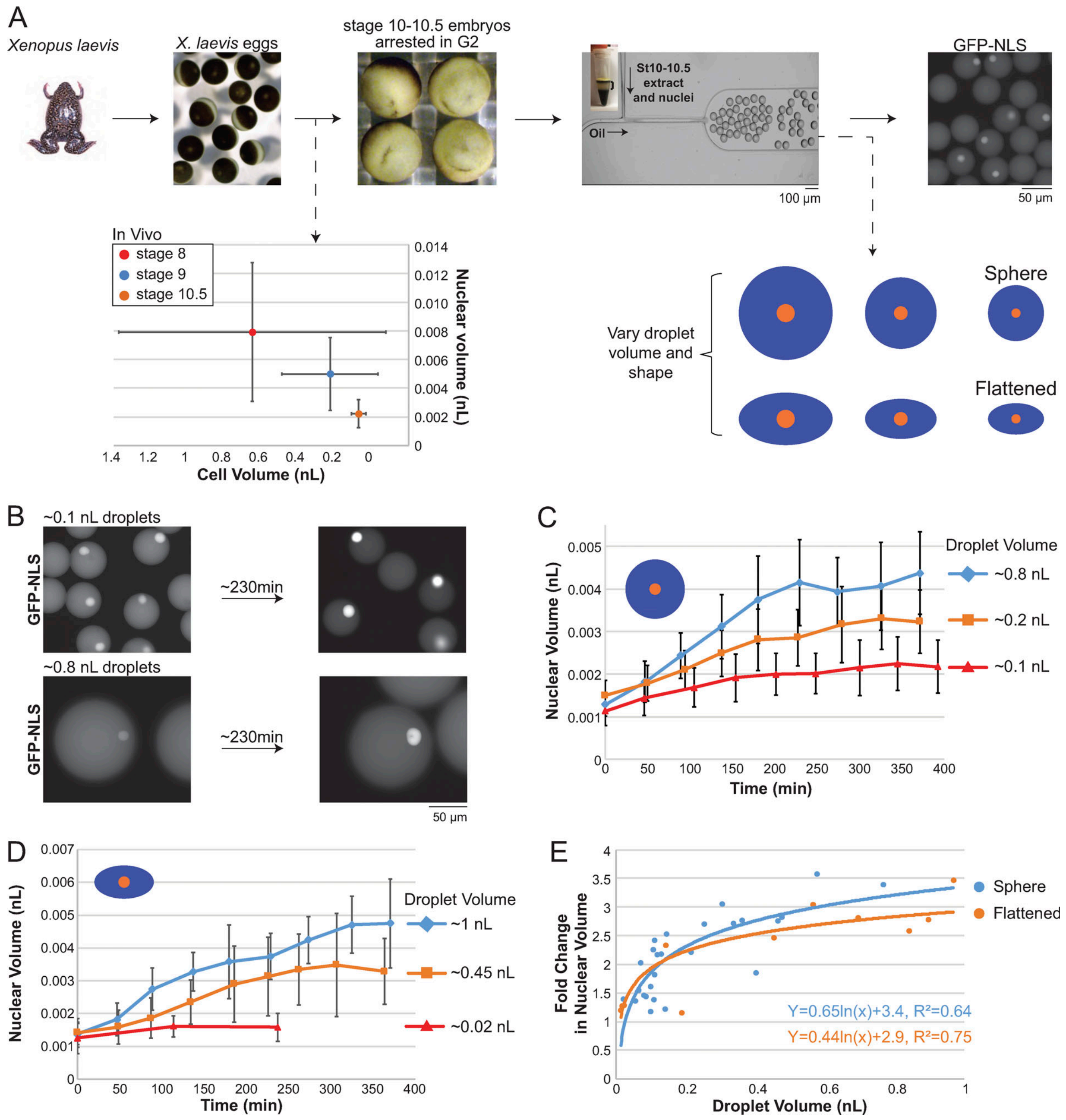

Figure 1. **Cytoplasmic volume contributes to nuclear size scaling in *X. laevis* embryo extracts. (A)** Top: Schematic diagram of the experimental approach. Stage 10–10.5 embryos were arrested in late interphase with cycloheximide. Embryonic extract containing endogenous nuclei was encapsulated in droplets using microfluidic devices. Nuclei were visualized by uptake of GFP-NLS. Bottom left: In vivo nuclear size scaling data for *X. laevis* stages 8 to 10.5 (Jevtić and Levy, 2015). Bottom right: Blue and orange represent cytoplasm and nuclei, respectively. **(B)** Spherical extract droplets were incubated at room temperature. **(C)** Spherical droplet data. At each time point, 18–104 nuclei were quantified (57 nuclei on average). Each curve corresponds to a different extract. **(D)** Flattened droplet data. The ratio of the long axis to the short axis was on average ~1.7. At each time point, 10–117 nuclei were quantified (35 nuclei on average). Each curve corresponds to a different extract. **(E)** The fold change in nuclear volume was calculated by dividing maximum nuclear volume by initial nuclear volume at t = 0. Best-fit logarithmic regression curves are displayed. For each time point of each experiment, 7–311 nuclei were quantified (63 nuclei on average). Data are shown for 26 different spherical droplet volumes (blue) and 12 different flattened droplet volumes (orange), using 23 different extracts. Error bars represent SD.

encapsulation. We first performed high-speed fractionation of egg extract and determined that the nuclear growth-inducing activity was present in cytosol, but not in the heavy or light membrane fractions (Fig. 3 A). We also determined that nuclear growth was dependent on importin α/β-mediated import, because cytosol treated with the importin β-binding domain of importin α (IBB) failed to induce growth of stage 10 nuclei (Fig. 3 A). Consistent with this finding, nuclei also failed to grow in stage 10 extract droplets when import was blocked with IBB or wheat germ agglutinin (Fig. 3 B).

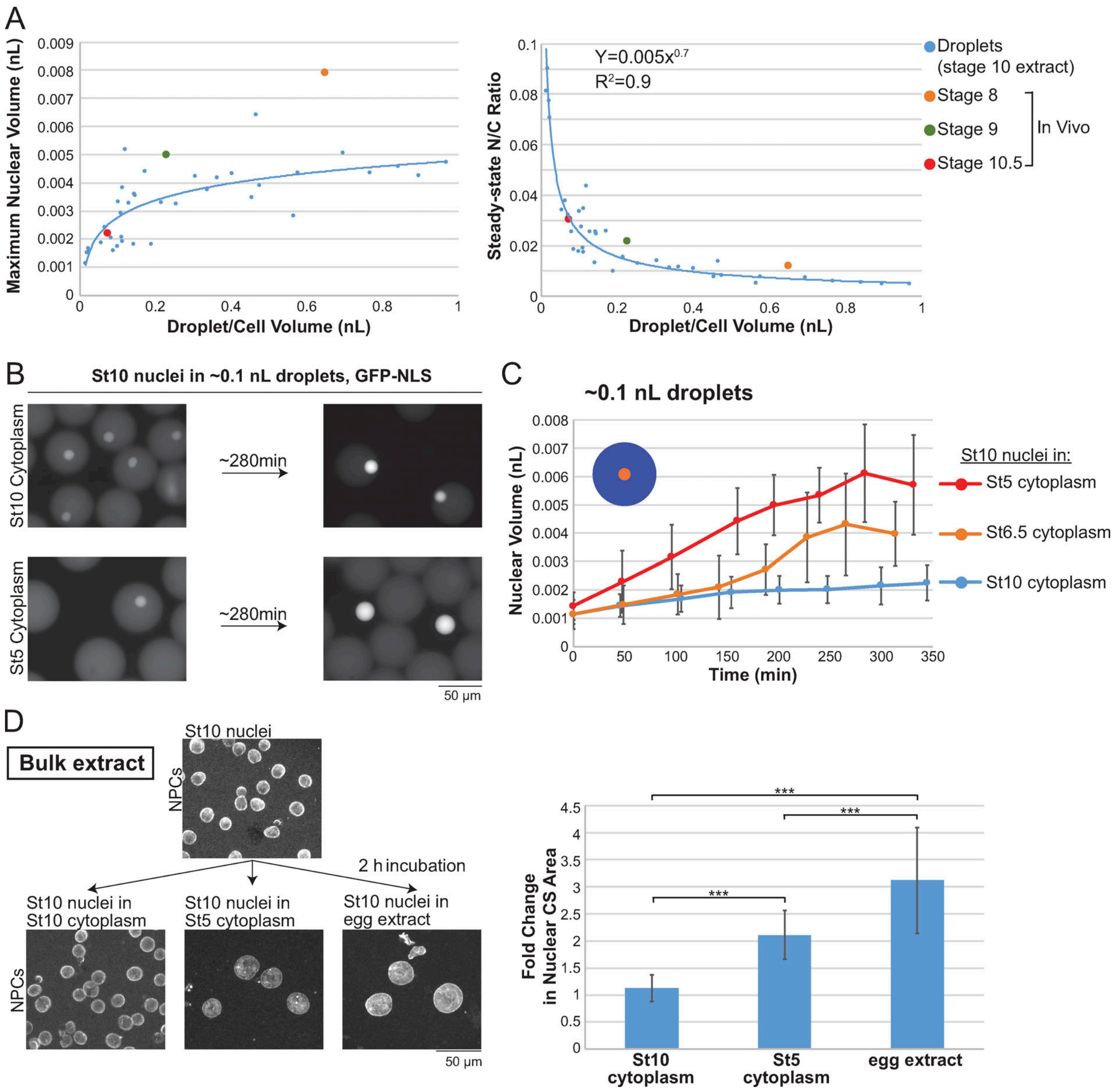

Figure 2. **Cytoplasmic composition contributes to nuclear size scaling in *X. laevis* embryo extracts. (A)** Left: Based on the data presented in Fig. 1, C–E, maximum nuclear volume is plotted as a function of droplet volume for stage 10 embryo extract droplets (blue). Right: Nuclear-to-cytoplasmic (N/C) volume ratios were calculated by dividing maximum nuclear volume by droplet volume. A best-fit power regression curve is displayed for the droplet data. Also plotted are previously reported in vivo nuclear size scaling data and nuclear-to-cytoplasmic volume ratios for *X. laevis* stages 8 to 10.5 (Jevtić and Levy, 2015). **(B)** Stage 10 nuclei were isolated and resuspended in cytoplasmic extract from different embryonic stages. Extract droplets were incubated at room temperature. **(C)** At each time point, 10–168 nuclei were quantified (80 nuclei on average). The stage 10 extract data are the same shown in Fig. 1 C. **(D)** Stage 10 extract and nuclei were mixed with stage 5 cytoplasmic extract or egg extract at a 1:10 ratio. After a 2-h incubation, nuclei were fixed and stained with NPC antibody mAb414. Nuclear CS areas were measured and the fold change was calculated relative to the preincubation nuclear size. At least 700 nuclei were quantified for each condition. Data from two independent experiments are shown. Two-tailed Student's *t* tests assuming equal variances; ***, $P \le 0.001$. Error bars represent SD.

Having determined that the nuclear growth activity was present in egg extract cytosol, we subjected cytosol to fractionation by gel filtration and ion exchange chromatography, monitoring fractions capable of inducing in vitro growth of stage 10 nuclei (Fig. 3, C and D). We ultimately identified two active fractions (Fig. 3 D), and we determined the protein composition of these fractions by mass spectrometry (Fig. S2, A and B). Because the nuclear growth activity was dependent on nuclear import (Fig. 3, A and B), we focused on the most abundant proteins with NLSs. We were struck by the fact that nucleoplasmin (Npm2) was identified in both fractions (Fig. 3 D and Fig. S2, B and C). Npm2 is a pentameric histone chaperone that binds core histones and promotes their assembly into nucleosomes (Frehlick et al., 2007; Platonova et al., 2011). We suspect that it eluted in two different ion exchange chromatography fractions due to its association with different protein complexes. Consistent with this idea, mass spectrometry identified core histones in only the lower salt Npm2 elution (data not shown).

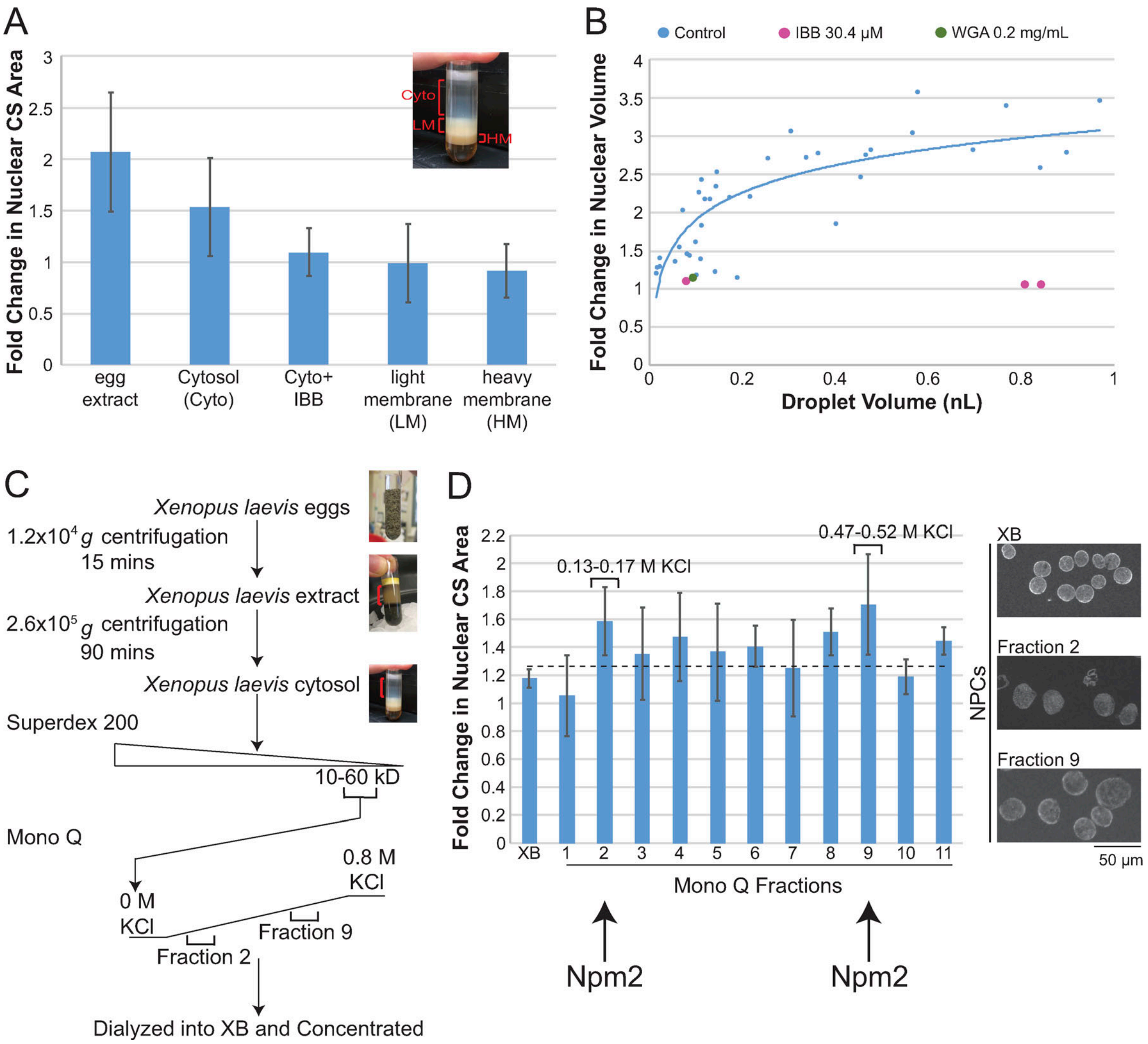

Figure 3. **Fractionation approach to identifying factors limiting for nuclear growth. (A)** *X. laevis* egg extract was subjected to high-speed centrifugation to separate the extract into cytosol (Cyto), light membrane (LM), and heavy membrane (HM). Stage 10 nuclei were incubated with the indicated fractions for 120 min. IBB, added at ∼30 µM, inhibits nuclear import (Weis et al., 1996). Nuclear CS areas were measured for at least 200 nuclei per condition and normalized to the preincubation nuclear size. Data from two independent experiments are shown. **(B)** Experiments were performed as in Fig. 1, C–E, except that extracts were supplemented with IBB or wheat germ agglutinin (WGA) to block nuclear import (Cox, 1992). For each experiment, 7–212 nuclei were quantified at each time point (53 nuclei on average). Data from three different extracts are shown. The control data are the same shown in Fig. 1 E. **(C)** Schematic diagram of the fractionation approach. See Materials and methods for details. **(D)** Mono Q fractions were dialyzed into XB and concentrated ∼10- to 20-fold. Stage 10 embryo extract and nuclei were supplemented with equivalent volumes of XB or Mono Q fractions and incubated for 90 min. Nuclei were fixed and stained with NPC antibody mAb414. Nuclear CS areas were measured and the fold change was calculated relative to the preincubation nuclear size. Means and SDs from three independent fractionation experiments are shown. At least 160 nuclei were quantified for each condition. The dotted line indicates the top of the error bar for the XB control. We selected fractions with the largest fold changes in nuclear size and with SD error bars above the dotted line, namely, fractions 2 and 9, which were shown by mass spectrometry to contain Npm2. Error bars represent SD.

We also determined that Npm2 is present in the cytoplasm of stage 10 extracts (Fig. S2 D), potentially explaining why increasing droplet volume and therefore the amount of available cytoplasmic Npm2, lead to nuclear growth. Although Npm2 lacks an obvious nuclear export signal, it likely still shuttles between the nucleus and cytoplasm to adopt a steady-state distribution (Kopito and Elbaum, 2007; Nguyen et al., 2019).

To test if Npm2 levels affect nuclear size in vivo, we microinjected one-cell *X. laevis* embryos and analyzed nuclei at stage 10–10.5. Increasing the Npm2 concentration by 3.5 µM induced an ∼1.3-fold increase in nuclear volume (Fig. 4 A). Npm2 is a known importin α/β cargo (Kim et al., 2017), and nuclear size was unaffected in embryos microinjected with Npm-core lacking the NLS (Fig. 4 A), demonstrating that nuclear import of Npm2 is required to have an effect on nuclear size. For embryos microinjected with Npm2 protein, Npm2 immunofluorescence revealed two populations of nuclei, one group with control level Npm2 staining and one group with on average approximately fourfold more intense Npm2 staining (Fig. 4 A), suggesting that microinjected Npm2 protein was not evenly distributed across the one-cell embryo. When we quantified nuclei with more intense Npm2 staining, we observed an ∼1.8-fold increase in

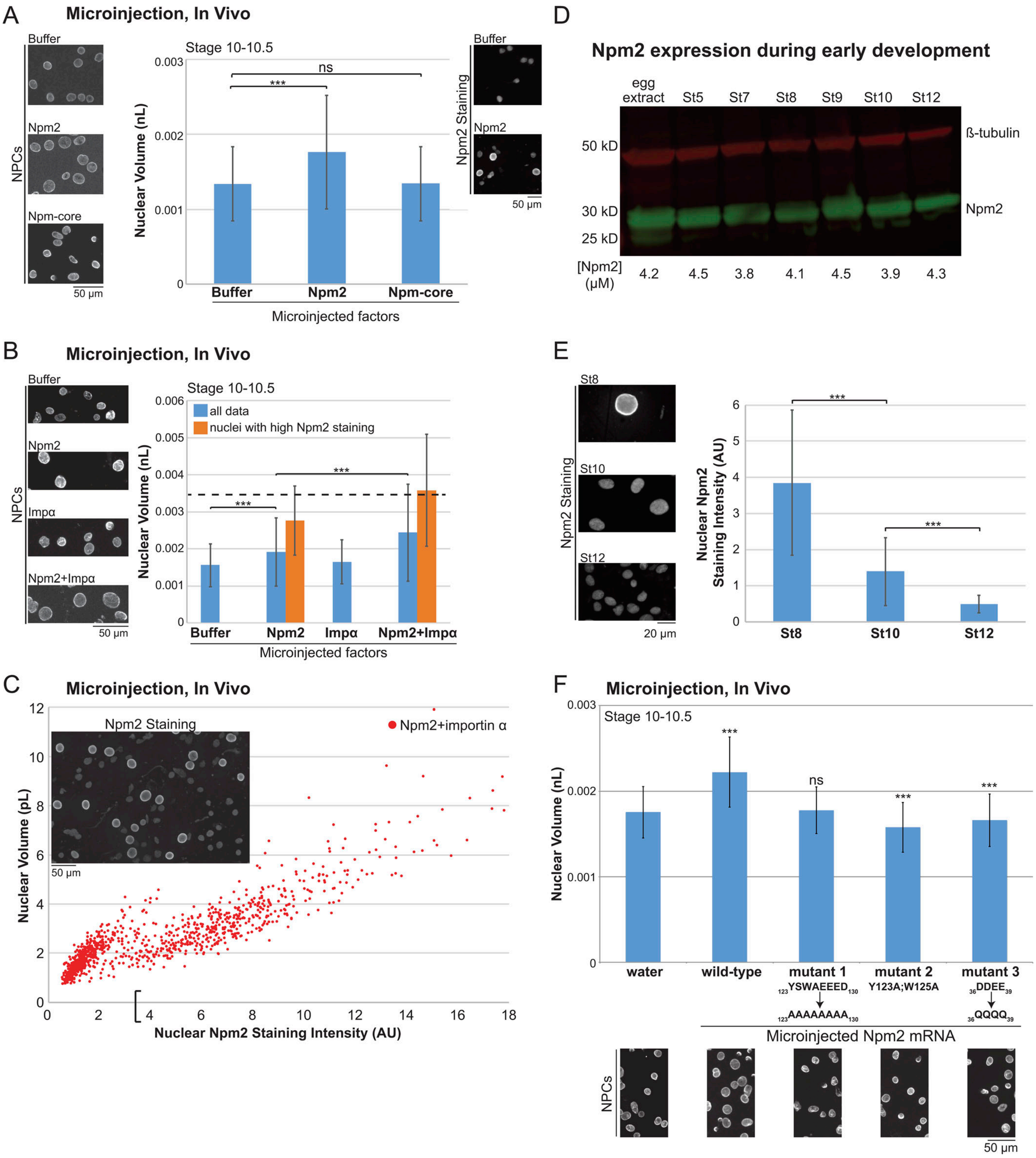

Figure 4. **Npm2 levels affect in vivo nuclear size. (A)** One-cell *X. laevis* embryos were microinjected with equivalent volumes of XB, recombinant Npm2 protein (to increase the Npm2 concentration by 3.5 µM) or recombinant Npm-core protein (3.5 µM final), allowed to develop to stage 10–10.5, and arrested in G2 with cycloheximide. Isolated nuclei were stained with an NPC antibody (mAb414), and nuclear volumes were measured for at least 74 nuclei per condition per experiment. 25 embryos on average were microinjected per condition. Data from four independent experiments and representative images are shown. Representative images to the right show nuclei stained with an antibody against Npm2. **(B)** Microinjections were performed as in A without cycloheximide arrest and including, where indicated, importin-α-E mRNA (350 pg total, Imp α). Importin-α-E is a phosphomimetic version of human importin α2 with reduced affinity for membranes (Levy and Heald, 2010; Wilbur and Heald, 2013). At least 330 nuclei were quantified per condition per experiment. Data from two independent experiments and representative images are shown. Orange bars represent sizes for nuclei with Npm2 staining intensity values >1 SD above the XB control (see also panel C). The dotted horizontal line at 3.5 pl corresponds to the predicted stage 10 nuclear volume resulting from a 3.5-µM introduction of Npm2 (see also Fig. S2 F). **(C)** Nuclei from microinjections described in B were stained with an antibody against Npm2. Nuclear volumes and total nuclear Npm2

staining intensities were measured for ≥330 nuclei per condition per experiment. 25 embryos on average were microinjected per condition, and two independent experiments were performed. For the Npm2 + importin α condition, individual nuclear volume was plotted as a function of nuclear Npm2 staining intensity. For XB-microinjected embryos, nuclear Npm2 staining intensity was 2.05 ± 1.35 (average ± SD). In panel B here and in Fig. S4 D, the orange bars represent data for nuclei with Npm2 staining intensity values greater than one SD above the XB control; therefore, nuclei with Npm2 staining intensities >2.05 + 1.35 = 3.4 (indicated by the open bracket on the x axis in C). **(D)** Equivalent volumes of egg and embryo extracts were analyzed by Western blot. Npm2 band intensities were normalized to β-tubulin levels and used to estimate the Npm2 concentration for each stage, given an egg extract Npm2 concentration of 4.2 µM. **(E)** Embryonic nuclei were stained for Npm2, and total nuclear Npm2 staining intensities were quantified for ≥148 nuclei per stage. **(F)** Microinjections were performed as in A with 1 ng of the indicated Npm2 mRNAs or an equivalent volume of water as a control. Mutants 1 and 2 have mutations in the histone-binding region of Npm2 (Warren et al., 2017), and mutant 3 is defective in histone chaperone activity (Salvany et al., 2004). We verified that these mutants are nuclear-import competent (data not shown). At least 900 nuclei were quantified per condition per experiment. Data from two independent experiments and representative images are shown. All statistical comparisons are to the water control. Two-tailed Student's *t* tests assuming equal variances; ***, P ≤ 0.001; ns, not significant. Error bars represent SD.

---

nuclear volume relative to controls (Fig. 4 B) and a strong positive correlation between nuclear volume and Npm2 nuclear staining intensity (Fig. 4 C). If Npm2 becomes limiting for nuclear size over the course of normal development, then we would expect the amount of Npm2 per cell to decrease. Indeed, we found that the total Npm2 concentration remains constant at ~4.2 µM from stage 5 to 12 (Figs. 4 D and S2 E), which predicts that per-cell amounts of Npm2 should decrease approximately ninefold from stage 8 to 10 (Fig. S2 F), consistent with Npm2 nuclear staining intensity measurements (Fig. 4 E). Interestingly, the total amount of nuclear Npm2 per embryo increases over development (Fig. S2 G), indicating that Npm2 is progressively depleted from the cytoplasm as nucleus number increases. Thus increasing the in vivo concentration of Npm2 is sufficient to increase nuclear size, and Npm2 reductions may contribute to developmental nuclear size scaling.

Based on the amount of Npm2 microinjected into embryos, the known in vivo Npm2 concentration, and known cell and nuclear sizes at different developmental stages, we predicted that 3.5 µM microinjected Npm2 would produce a stage 10 maximum nuclear volume of 0.0035 nl if Npm2 was the only factor limiting for nuclear growth (Fig. S2 F). Because microinjecting Npm2 alone was not sufficient to induce this predicted increase in nuclear volume (Fig. 4, A and B), we wondered if other activities might work additively with Npm2. We focused on importin α, because Npm2 is an importin α/β cargo (Kim et al., 2017) and reductions in the cytoplasmic levels of importin α, but not importin β, contribute to development nuclear size scaling (Brownlee and Heald, 2019; Levy and Heald, 2010; Wilbur and Heald, 2013). We microinjected embryos to increase levels of both Npm2 and importin α. While importin α alone had a minimal effect on nuclear size in stage 10 embryos, Npm2 and importin α together induced an ~1.6-fold increase in nuclear volume, and the increase was even larger at ~2.3-fold when considering nuclei with high Npm2 staining intensity (Fig. 4 B), with some nuclear volumes approaching the predicted value of 0.0035 nl. These data suggest that both cargos and transport factors limit nuclear growth in later development.

Our in vitro data support the idea that multiple factors are limiting for nuclear growth. Addition of Npm2 to encapsulated stage 10 extract only induced significant nuclear growth when supplemented with egg extract cytosol (Fig. S3, A–C), with 3.5 µM Npm2 causing the largest increase in nuclear size and Npm-core lacking its NLS having no effect (Fig. S3 D). Furthermore, we found that lamins, PKC, and importin α were not on their own sufficient to induce growth of stage 10 nuclei (Fig. S3, E–F); however, adding Npm2 in combination with lamin B3 promoted nuclear growth, with importin α and histones having more minor effects (Fig. S3 G). To address potential caveats of increasing Npm2 amounts, we inhibited Npm2 by supplementing extract with Npm2 neutralizing antibodies, which resulted in a modest reduction in nuclear growth and size (Fig. S3 H). Thus, Npm2 is one factor, among many, that limits growth of stage 10 nuclei.

Npm2 increases nuclear histone levels and chromatin compaction

How might Npm2 promote nuclear growth? Npm2 is a histone chaperone that facilitates the assembly of nucleosomes on chromatin (Earnshaw et al., 1980; Philpott et al., 1991) and nuclear import of histones (Gurard-Levin et al., 2014). Because Npm2 is very acidic, we wondered if nuclear growth might be due to import of a high-abundance, charged cargo. Using our in vitro assay, we tested 3.5 µM of a wide variety of nuclear imported cargos of varying charge, and none induced nuclear growth, including proliferating cell nuclear antigen and nucleolin, which have similar isoelectric points to Npm2 (Fig. S4 A). Furthermore, in embryos microinjected with Npm2 mutants defective for histone binding and/or histone chaperone activity but still import competent, nuclear growth was abrogated relative to wild-type Npm2 (Fig. 4 F). These data support the idea that Npm2 influences nuclear size through its histone chaperone activity rather than through a nonspecific charge effect.

To determine if there is a correlation between nuclear histone levels and nuclear size, we allowed nuclei to reach different sizes in *X. laevis* egg extract and observed that the nuclear H2B staining intensity increased as nuclei grew and chromatin appeared to occupy proportionately less of the nuclear space and to adopt a more heterogeneous distribution (Fig. 5 A). To quantify chromatin distribution, we drew line scans through the middle of Hoechst-stained nuclei and measured the SD of intensity values along these lines. We termed this parameter the "chromatin heterogeneity index," with larger values corresponding to more heterogeneous chromatin distributions. As nuclei grew in egg extract, the chromatin heterogeneity index increased (Fig. 5 A). We also measured the area occupied by Hoechst-staining chromatin normalized to nuclear area and termed this parameter the "chromatin relative area" (Baarlink et al., 2017), finding

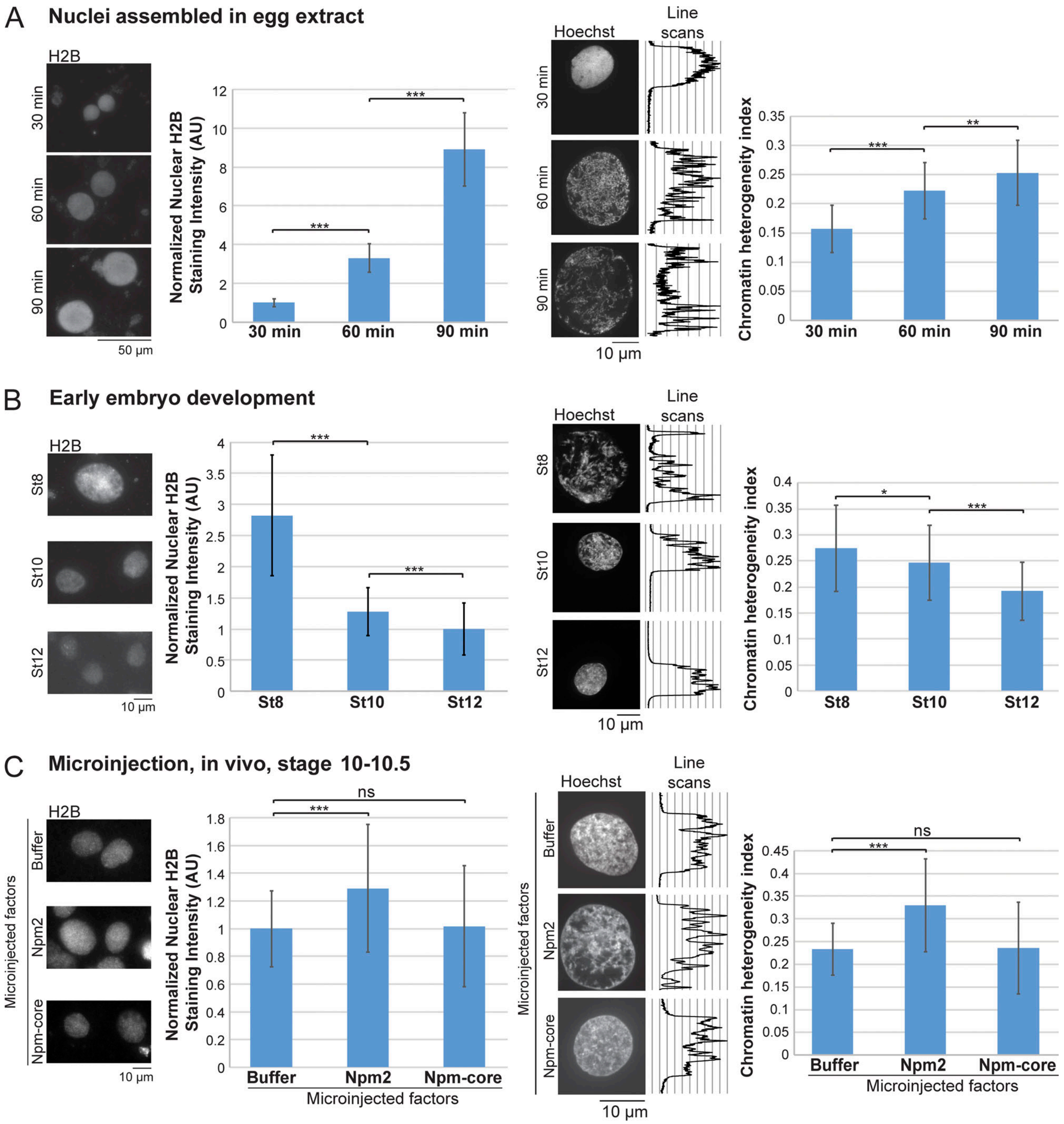

Figure 5. **Npm2 levels correlate with nuclear histone levels and altered chromatin topology. (A)** Nuclei assembled in *X. laevis* egg extract for 30, 60, and 90 min were stained with an H2B antibody and Hoechst. Total nuclear H2B staining intensities were measured for ≥60 nuclei per condition and normalized to the 30-min time point. For each nucleus, two Hoechst intensity line scans were acquired through the middle of the nucleus. The SD of all intensity values along each line was calculated and normalized to the average intensity to obtain a value we term the chromatin heterogeneity index. Larger values correspond to a more heterogeneous chromatin distribution. 54–68 line scans were quantified per condition (60 on average). **(B)** Different stage nuclei were stained with an H2B antibody and Hoechst. Total nuclear H2B staining intensities were quantified for ≥100 nuclei per stage and normalized to stage 12. For chromatin heterogeneity indexes, 22–79 line scans were quantified per condition (45 on average). **(C)** Microinjection experiments were performed as in Fig. 4 A. Isolated nuclei were stained with an H2B antibody and Hoechst. Total nuclear H2B staining intensities were measured for ≥97 nuclei per condition and normalized to the XB-microinjected controls. For chromatin heterogeneity indexes, 34–52 line scans were quantified per condition (41 on average). Data from four independent experiments are shown. Two-tailed Student's *t* tests assuming equal variances; *, P ≤ 0.05; **, P ≤ 0.01; ***, P ≤ 0.001; ns, not significant. Error bars represent SD.

that it decreased by more than twofold as nuclei expanded (Fig. S4 B). These data suggest that nuclear growth is accompanied by increased nuclear histone accumulation and changes in chromatin organization.

We next examined whether a similar trend might accompany reductions in nuclear size during development. As per-cell amounts of Npm2 decrease over development (Figs. 4 D and S2 F), we observed a reduction in both nuclear H2B staining intensity and the chromatin heterogeneity index, while chromatin relative area increased (Figs. 5 B and S4 C). In embryos microinjected to increase Npm2 levels, concomitant with an increase in nuclear size, we observed more nuclear H2B staining, an increased chromatin heterogeneity index, and decreased chromatin relative area (Figs. 5 C and S4 D). None of these effects were observed when Npm-core was microinjected (Figs. 5 C and S4 D), and similar results were observed in vitro (Figs. S3 D and S4 E). To determine if these Npm2-induced changes in chromatin organization were due to altered nucleosome assembly, we performed micrococcal nuclease (MNase) digestion assays. Nucleosome occupancy was increased in embryos microinjected with either Npm2 protein or mRNA (Fig. 6, A and B). Furthermore, this increase in chromatin compaction was associated with a reduction in histone H3 acetylation, indicating a reduction in euchromatin (Fig. 6 C). Thus, at the scale of both bulk chromatin and nucleosomes, Npm2 promotes chromatin compaction with concomitant increases in nuclear size.

Because histone chaperones also play important roles in transcriptional regulation (Gurard-Levin et al., 2014), we tested if the ability of Npm2 to promote nuclear growth was transcription dependent. Nuclear growth induced by the addition of Npm2 still occurred in the presence of α-amanitin, an inhibitor of RNA polymerase II and III transcription (Fig. S4 F), indicating transcriptional changes are not required for Npm2 to increase nuclear size. This is consistent with Npm2 inhibition decreasing nuclear size in *X. laevis* egg extract, which is transcriptionally inert (Fig. S3 H). Taken together, we propose that Npm2 promotes nuclear growth independently of transcription by increasing nuclear histone levels and chromatin compaction, in turn impacting higher-order chromatin structure and distribution within the nucleus.

Discussion

Npm2 is a developmental nuclear size scaling factor

Our data support the model that reductions in cytoplasmic volume and limiting components contribute to developmental nuclear size scaling. We identify Npm2 as a nuclear size effector and potential limiting component. Per-cell amounts of Npm2 decrease over *X. laevis* development, as expected for a factor that might become limiting for nuclear growth, and increasing the in vivo Npm2 concentration was sufficient to increase nuclear size. We believe the identification of Npm2 as a nuclear size effector is novel because it is a nucleoplasmic/volumetric factor, as opposed to previously identified surface area nuclear size regulators that are structural components of the NE, such as lamins, lamina-associated proteins, and nesprins (Jevtić and Levy, 2014; Mukherjee et al., 2016; Webster et al., 2009).

Why might Npm2 become physiologically limiting in vivo in post-MBT embryos? In the egg, Npm2 binds to and sequesters maternal core histone stores (Onikubo et al., 2015). In pre-MBT embryos, Npm2 and histones are presumably in large excess to the number of nuclei, which explains why supplementing *X. laevis* egg extract with recombinant Npm2 did not increase nuclear size (Levy and Heald, 2010). At the MBT, while the Npm2 concentration remains constant, core histone levels increase (Peshkin et al., 2015; Sun et al., 2014), meaning the Npm2/histone ratio decreases in post-MBT embryos. Furthermore, bulk nuclear import kinetics decrease over development (Levy and Heald, 2010). As a result, limiting amounts of Npm2 are imported more slowly, correlating with reductions in nuclear size. Thus, Npm2 levels and import kinetics both contribute to nuclear size scaling over development.

Npm2 does not fully account for developmental reductions in nuclear size. Our extract encapsulation experiments showed that other cytosolic components, such as lamin B3, were necessary for Npm2 to induce an upward shift in the nuclear size–scaling curve, and increasing Npm2 levels in vivo was not sufficient to achieve nuclear sizes characteristic of pre-MBT developmental stages. We observed additive effects when Npm2 levels were manipulated along with importin α. It is worth noting that increasing importin α levels alone enhances nuclear growth in pre-MBT embryos (Jevtić and Levy, 2015; Levy and Heald, 2010), but not in post-MBT embryos, where overexpression of both importin α and Npm2 was required. Perhaps import limits nuclear growth in early embryos while the availability of nuclear-sizing cargos becomes limiting later. Npm2 does not possess an obvious nuclear export signal and stage 10 nuclear size is not sensitive to leptomycin B treatment (Edens and Levy, 2014), suggesting active export is not a major determinant of nuclear size at this developmental stage. However, Npm2 has been demonstrated to shuttle between the cytoplasm and nucleus (Kopito and Elbaum, 2007), as have many histone chaperones (Keck and Pemberton, 2013), and it is common for proteins with an NLS to exhibit dynamic nucleocytoplasmic partitioning even at steady state (Kırlı et al., 2015; Nguyen et al., 2019; Wühr et al., 2015). Given these observations, increased importin α may drive nuclear growth by directly increasing Npm2 nuclear import, although importin α likely also promotes import of other nuclear-sizing cargos secondarily to Npm2, such as lamin B3. Thus, it is necessary to invoke multiple mechanisms to fully account for the reductions in nuclear size that occur during early development.

Mechanism of Npm2 action on nuclear size

While Npm2 influences nuclear size independently of transcription, open questions remain about precisely how Npm2 promotes nuclear growth. Nuclear pore complex (NPC) assembly is known to require nucleosomes (Inoue and Zhang, 2014; Zierhut et al., 2014), so one possibility is that increased nucleosome assembly by Npm2 leads to larger numbers of NPCs and increased nuclear import capacity. We disfavor this model because growth of stage 10 nuclei with egg cytosol did not lead to an increase in NPC density, and NPC staining intensity was not significantly altered in Npm2-microinjected embryos and was

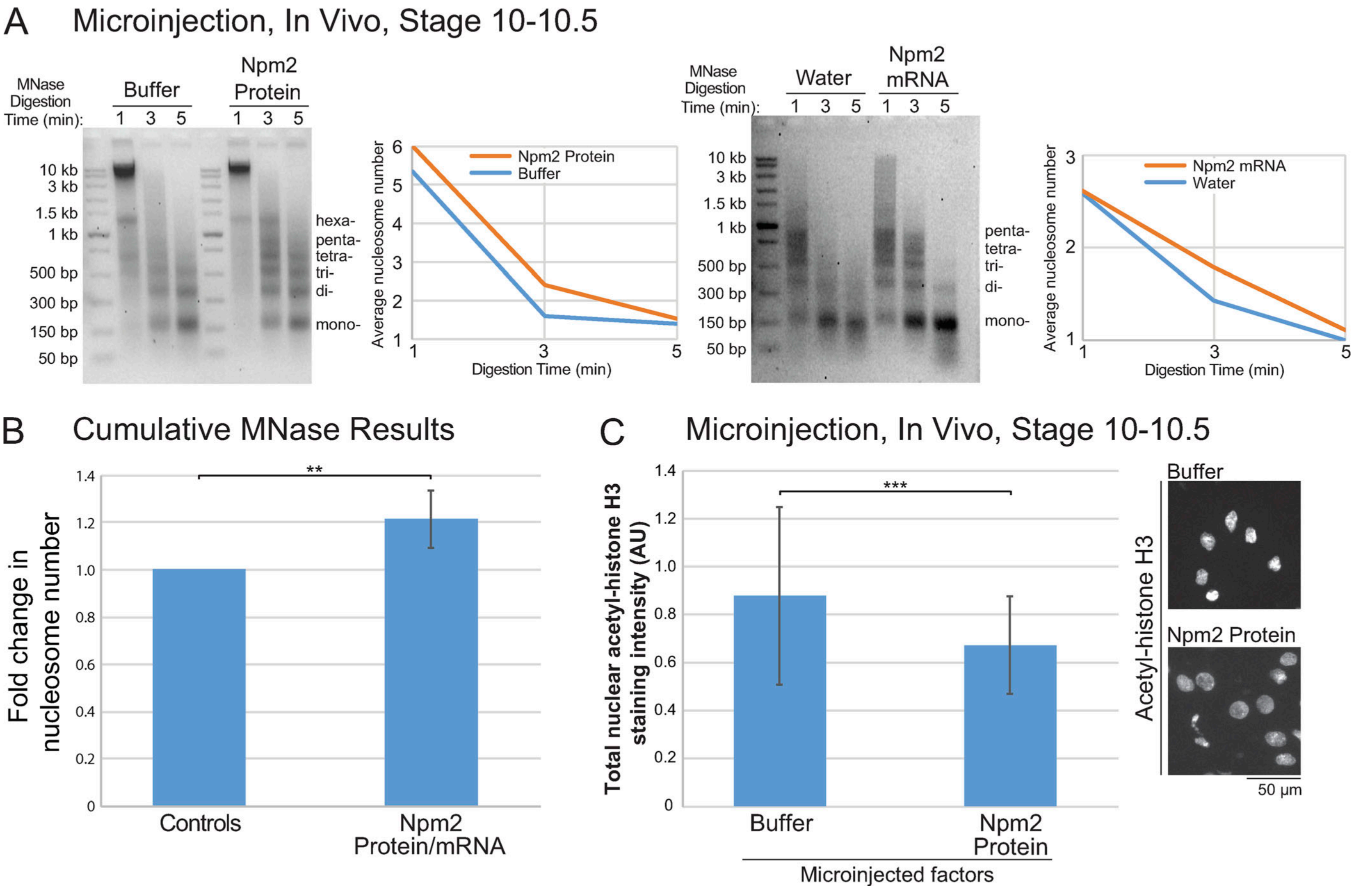

Figure 6. **Npm2 increases nucleosome occupancy and decreases euchromatin. (A)** On the left, one-cell *X. laevis* embryos were microinjected with equivalent volumes of XB or recombinant Npm2 protein (to increase the Npm2 concentration by 3.5 µM). On the right, one-cell *X. laevis* embryos were microinjected with 1 ng wild-type Npm2 mRNA or an equivalent volume of water. Embryos were allowed to develop to stage 10–10.5 and arrested in G2 with cycloheximide. Isolated nuclei were digested with MNase for the indicated times, and purified DNA was separated on 2% agarose gels and stained with ethidium bromide. On average, 60 embryos were microinjected per condition. Band intensities were quantified and used to calculate the average nucleosome number per fragment (see Materials and methods). Representative experiments are shown. **(B)** The MNase digestion assays described in A were repeated three times for Npm2 protein microinjection and three times for Npm2 mRNA microinjection. Maximum fold changes in nucleosome occupancy between control and Npm2-microinjected embryos were quantified for each experiment and averaged. **(C)** One-cell *X. laevis* embryos were microinjected with equivalent volumes of XB or recombinant Npm2 protein (to increase the Npm2 concentration by 3.5 µM), allowed to develop to stage 10–10.5, and arrested in G2 with cycloheximide. On average, 25 embryos were microinjected per condition. Isolated nuclei were stained with an acetyl-histone H3 antibody, and representative images are shown. Total integrated nuclear acetyl-histone H3 staining intensity was measured for ≥168 nuclei per condition. One representative experiment of two is shown. Two-tailed Student's *t* tests assuming equal variances; **, $P \le 0.01$; ***, $P \le 0.001$. Error bars represent SD.

not greater for nuclei with high Npm2 staining (data not shown). Another possibility is that increased bulk import of Npm2 and histones leads to passive nuclear enlargement due to increased intranuclear protein content. We disfavor that model because (1) other similarly charged cargos failed to induce nuclear growth, (2) particularly high Npm2 concentrations had a dominant-negative effect on nuclear size, and (3) nuclear growth was dependent on Npm2's histone chaperone activity.

We favor a model in which Npm2 induces nuclear growth by increasing nuclear histone localization, nucleosome assembly, and chromatin compaction. Previous studies have shown that large-scale chromatin decompaction induced by knockdown of histone H1, condensins, or MeCP2 can lead to nuclear enlargement (Bustin and Misteli, 2016), while we find that Npm2-induced chromatin compaction drives nuclear growth. Potential explanations for these differing results include (1) differences in cell type or developmental stage, (2) differing effects of a histone chaperone as opposed to bulk chromatin structural and binding proteins, or (3) indirect effects of protein knockdown on nuclear size resulting from delayed cell cycle progression or altered gene expression. It is also possible that there are two distinct regimes of chromatin packing that both lead to increased nuclear size. Extreme decompaction induced by knockdown of chromatin structural and binding proteins might increase nuclear size because the DNA occupies a much larger volume. On the other hand, subtle chromatin compaction by Npm2 under more normal physiological conditions might also drive nuclear growth.

Why might increased nucleosome assembly and chromatin compaction promote nuclear growth? While changes in nucleosome assembly might affect chromatin–NE interactions and/or chromatin association of linker histones and chromatin binding/

remodeling proteins, it is also well established that more condensed chromatin is stiffer (Chalut et al., 2012; Stephens et al., 2017, 2018). Chromatin stiffness increases with histone levels and nucleosome packing as a result of increased interactions between adjacent histone tails (Shimamoto et al., 2017). We propose that stiffer chromatin tends to occupy a larger nuclear volume, akin to cellular tensegrity (tensional integrity) models of cellular architecture (Aranda-Anzaldo, 2016; Ingber, 2003). Consistent with observed large chromatin movements (Zidovska et al., 2013), a stiffer chromatin fiber might exert a greater force on the NE and perhaps promote protein incorporation into the nuclear lamina that would stabilize nuclear expansion. Thus, while extranuclear mechanical forces are known to impact nuclear function (Kirby and Lammerding, 2018), here we propose a role for intranuclear forces in NE expansion.

Histone chaperones and nuclear size in development and cancer

Our model that Npm2 is a nuclear size–scaling factor over development is consistent with known developmental changes in histone occupancy and transcription. As embryos approach the MBT and total DNA content in the embryo rapidly increases, histone titration is one mechanism that contributes to the upregulation of zygotic transcription (Amodeo et al., 2015; Onikubo and Shechter, 2016). Reduced nucleosome assembly and increased transcription at the MBT correlate with less condensed chromatin (Bogdanović et al., 2012; Hontelez et al., 2015), which by our model is predictive of reduced nuclear size during developmental progression. Because Npm2 belongs to a large family of nucleophosmin/Npm2 histone chaperones that are conserved throughout metazoans (Frehlick et al., 2007), it will be important to determine if other histone chaperones impact nuclear size and whether such mechanisms are conserved in other systems. Of note, eight-cell-stage Npm2-null mouse embryos exhibited smaller nuclei than wild type as well as a loss of heterochromatin and altered chromatin organization (Burns et al., 2003). Lastly, histone chaperones have been implicated in cancer (Burgess and Zhang, 2013; Grisendi et al., 2006), and future work will address the complex relationships among chromatin structure, nuclear size, and disease pathology.

Materials and methods

X. laevis embryos, extracts, and microinjections

X. laevis embryos were obtained as previously described (Sive et al., 2000). Freshly laid *X. laevis* eggs were in vitro fertilized with crushed *X. laevis* testes. Embryos were dejellied in 3% cysteine (wt/vol), pH 7.8, dissolved in 1/3× MMR (1× MMR: 0.1 mM EDTA, 0.1 M NaCl, 2 mM KCl, 2 mM $CaCl_2$, 1 mM $MgCl_2$, and 5 mM Hepes, pH 7.8). Embryos were developed in 1/3× MMR, staged (Nieuwkoop and Faber, 1967), and arrested in late interphase with 0.15 mg/ml cycloheximide for 60 min unless otherwise indicated (Lemaitre et al., 1998). Embryo extracts were prepared as previously described (Edens and Levy, 2014, 2016). Briefly, arrested embryos were washed several times in ELB (50 mM KCl, 2.5 mM $MgCl_2$, 250 mM sucrose, and 10 mM Hepes, pH 7.8) containing LPC (10 µg/ml each leupeptin, pepstatin, and chymostatin). For the final wash, the buffer was supplemented with 0.1 mg/ml cytochalasin D and 0.1 mg/ml cycloheximide. The embryos were packed in a tabletop centrifuge at 200 *g* for 1 min at room temperature, and excess buffer was removed. The embryos were crushed with a pestle and centrifuged at 10,000 *g* for 10 min at 16°C. The cytoplasmic extract containing endogenous embryonic nuclei was collected and supplemented with LPC, 0.02 mg/ml cytochalasin D, 0.1 mg/ml cycloheximide, and energy mix (3.8 mM creatine phosphate disodium, 0.5 mM ATP disodium salt, and 0.5 mM $MgCl_2$). Extracts were stored on ice until use. In some experiments, stage 10 nuclei were isolated by adding 1 ml ELB to 10–50 µl stage 10 extract, centrifuging at 1,600 *g* for 3 min to pellet nuclei, and removing the supernatant. It is worth noting that nuclear sizes vary significantly within stage 10–10.5 embryos (Jevtić and Levy, 2015), likely accounting for the relatively large standard deviation error bars observed in many of our nuclear size plots.

For microinjections, one-cell embryos were dejellied 30 min after fertilization, transferred to 1/3 MMR containing 2.5% Ficoll (wt/vol), and microinjected with 10–14-nl volumes using a PicoSprizer III (Parker). To estimate the protein concentration introduced by microinjection, we assumed an egg cytoplasmic volume of 0.5 µl. Microinjected embryos were allowed to develop in 1/3 MMR plus 2.5% Ficoll for 1 h and then transferred to 1/3 MMR for further development. Extracts from microinjected embryos were prepared as described above using ≥25 embryos. All *X. laevis* procedures and studies were conducted in compliance with the US Department of Health and Human Services *Guide for the Care and Use of Laboratory Animals*. Protocols were approved by the University of Wyoming Institutional Animal Care and Use Committee (assurance A-3216-01).

Encapsulation of *X. laevis* extract in microfluidic devices

X. laevis embryo extract encapsulation experiments were performed in polydimethylsiloxane (PDMS) microfluidic devices using T-junction droplet generators as previously described (Hazel et al., 2013; Oakey and Gatlin, 2018). PDMS (Sylgard 184; Dow Corning) microfluidic devices were replicated from a negative photoresist-on-silicon master using standard soft lithography protocols (Duffy et al., 1998). Device depth was determined by the thickness to which photoresist was spin-coated upon the silicon wafer. Devices with discrete reservoir depths of 15, 62, 85, and 120 µm were used in this study to achieve droplets of different shape. PDMS replicas were trimmed and holes were punched using sharpened blunt syringe tips. Prepared devices were exposed to an oxygen plasma (Harrick Plasma) and placed in conformal contact with a glass coverslip. After baking for 10 min at 70°C, an irreversible bond was formed between the PDMS and glass, allowing sealed devices to be used as fluidic networks.

For most experiments, extracts containing cytoplasm and endogenous nuclei were prepared from stage 10–10.5 embryos. To visualize nuclei, extracts were supplemented with 0.04–0.14 mg/ml recombinant GST-GFP-NLS or GST-mCherry-NLS. To limit liquid permeability through the PDMS walls, devices were submerged in ELB for 2 h before encapsulation and during imaging. *X. laevis* embryo extract and carrier oil (Pico-

Surf 2, 2% in Novec 7500; catalog no. 3200282; Dolomite Microfluidics) were loaded into separate syringes and connected to their respective channel inlets via Tygon microbore tubing (0.010-inch inside diameter × 0.030-inch outside diameter; catalog no. AAD04091; Saint-Gobain Performance Plastics). Fluid flow to the device was established using a syringe pump (neMYSYS, Cetoni, Chemyx; Kent Scientific). Generally, oil and extract flow rates were 1–10 µl/min and 0.1–1 µl/min, respectively. Relative flow rates were adjusted to vary droplet volume. Filled devices were sealed with acrylic nail polish, and droplets were stored in microfluidic reservoirs for imaging. Devices were filled and stored at 4°C before imaging at room temperature. Flattened droplet volumes were calculated as follows, where D_a is the apparent diameter of the droplet and D_d is the device depth:

$$V = (\pi \times D_d/2)^2 \times [(D_a - D_d)/2 + 2 \times D_d/3\pi] + \pi \times D_d \times [(D_a - D_d)/2]^2.$$

X. laevis egg extract, nuclear assembly, and fractionation

X. laevis metaphase-arrested egg extract (Good and Heald, 2018) and demembranated sperm chromatin (Hazel and Gatlin, 2018) were prepared as previously described. Freshly prepared egg extract was supplemented with LPC, cytochalasin D, and energy mix. De novo nuclear assembly was performed as previously described (Chen and Levy, 2018). Interphase-arrested egg extract was generated by supplementation with 0.6 mM $CaCl_2$ and 0.15 mg/ml cycloheximide followed by a 25-min room temperature incubation. Only extracts capable of robust nuclear assembly were used.

For fractionation, interphase-arrested egg extracts were centrifuged in a Beckman TL-100 centrifuge for 90 min at 55,000 rpm using a Beckman TLS-55 rotor at 4°C to generate cytosol, light-membrane, and heavy-membrane layers. The cytosol layer was collected and filtered (0.22-µm pore size, 13-mm cellulose acetate syringe filter). 0.8–1.0 ml of filtered cytosol was loaded onto a Superdex 200 10/300 GL column (GE Healthcare) equilibrated in XB (100 mM KCl, 0.1 mM $CaCl_2$, 1 mM $MgCl_2$, 50 mM sucrose, and 10 mM Hepes, pH 7.8). An Akta Purifier FPLC (GE Healthcare) was used to fractionate the cytosol into 40–0.4 ml fractions. Activity assays were performed by supplementing 5 µl of stage 10 embryo extract with 1 µl of each fraction or XB as a control and incubating at room temperature for 90 min, followed by nuclear fixation, imaging and cross-sectional (CS) area quantification as described in the Immunofluorescence and microscopy section. Active fractions were selected that induced a >14% increase in nuclear CS area relative to XB controls. Active fractions were collected and loaded on a Mono Q 5/50 GL (GE Healthcare) anion exchange chromatography column. Bound proteins were eluted using a 0–0.8-M KCl linear gradient in XB over a 6-ml volume, and 0.3-ml fractions were collected. Each fraction was dialyzed against XB buffer for ∼2 h at 4°C (3.5-kD cutoff; catalog no. 69550; Thermo Fisher Scientific) and concentrated 10- to 20-fold using centrifugal filter devices (Microcon YM-10, catalog no. 42407; Millipore) at 14,000 *g* for 30–60 min at 4°C. Activity assays were again performed, and active fractions were subjected to mass spectrometry for protein identification. Overall, the fractionation was repeated three separate times with roughly similar activity elution profiles.

For immunoinhibition, nuclei were assembled in interphase *X. laevis* egg extract using demembranated *X. laevis* sperm chromatin. Antibodies were dialyzed into XB, and extract was supplemented with equivalent volumes of XB or antibody. Control antibodies included anti-GFP (catalog no. A6455; Invitrogen) and anti-mCherry (RPCA-mCherry; EnCor Biotechnology). Two different *X. laevis* anti-Npm2 antibodies were tested, one that recognizes the Npm2 tail and one that recognizes the Npm2 core (Warren et al., 2017; both gifts from David Shechter, Albert Einstein College of Medicine, Bronx, NY). Final antibody concentrations ranged from 1.2 to 2.1 mg/ml. After incubating 90 min at room temperature, nuclei were fixed, isolated, stained with an anti-NPC antibody (mAb414), imaged, and quantified for nuclear CS area as described in the Immunofluorescence and microscopy section.

Protein sequence analysis and identification by liquid chromatography tandem mass spectrometry

Active fractions were separated on a 10% SDS-PAGE gel and stained with Coomassie. Gel bands were excised and submitted to the Taplin Mass Spectrometry Facility (Cell Biology Department, Harvard Medical School) for protein identification. Excised gel bands were cut into ∼1-mm³ pieces. Gel pieces were then subjected to a modified in-gel trypsin digestion procedure (Shevchenko et al., 1996). Gel pieces were washed and dehydrated with acetonitrile for 10 min followed by removal of acetonitrile. Pieces were then completely dried in a speed-vac. Rehydration of the gel pieces was with 50 mM ammonium bicarbonate solution containing 12.5 ng/µl modified sequencing-grade trypsin (Promega) at 4°C. After 45 min, the excess trypsin solution was removed and replaced with 50 mM ammonium bicarbonate solution to just cover the gel pieces. Samples were then placed in a 37°C room overnight. Peptides were later extracted by removing the ammonium bicarbonate solution, followed by one wash with a solution containing 50% acetonitrile and 1% formic acid. The extracts were then dried in a speed-vac (∼1 h) and stored at 4°C until analysis. Solution samples were reduced with 1 mM DTT (in 50 mM ammonium bicarbonate) for 30 min at 60°C. The samples were then cooled to room temperature, and 5 mM iodoacetamide (in 50 mM ammonium bicarbonate) was added, followed by a 15-min incubation in the dark at room temperature. DTT was then added to 5 mM to quench the reaction. Sequence grade trypsin was added at 5 ng/µl, and digestion performed overnight at 37°C. The samples were then desalted using an in-house-made desalting column.

On the day of analysis, the samples were reconstituted in 5–10 µl HPLC solvent A (2.5% acetonitrile and 0.1% formic acid). A nanoscale reverse-phase HPLC capillary column was created by packing 2.6-µm C18 spherical silica beads into a fused silica capillary (100-µm inner diameter × ∼30-cm length) with a flame-drawn tip (Peng and Gygi, 2001). After equilibrating the column, each sample was loaded via a Famos auto sampler (LC Packings) onto the column. A gradient was formed, and peptides were eluted with increasing concentrations of solvent B (97.5%

acetonitrile and 0.1% formic acid). As peptides eluted, they were subjected to electrospray ionization, and then they entered into an LTQ Orbitrap Velos Pro ion-trap mass spectrometer (Thermo Fisher Scientific). Peptides were detected, isolated, and fragmented to produce a tandem mass spectrum of specific fragment ions for each peptide. Peptide sequences (and hence protein identity) were determined by matching protein databases with the acquired fragmentation pattern by the software program Sequest (Thermo Fisher Scientific; Eng et al., 1994). All databases include a reversed version of all the sequences, and the data were filtered to between a 1% and 2% peptide false discovery rate.

Proteins

Recombinant GST-GFP-NLS, lamin A, lamin B1, lamin B3, and PKC βII-ΔNPS were expressed and purified as previously described (Edens et al., 2017; Jevtić et al., 2015; Levy and Heald, 2010). The mCherry sequence was amplified from pEmCherry-C2 (a gift from Anne Schlaitz, University of Heidelberg, Heidelberg, Germany) by PCR and cloned into pMD49 (a gift from Mary Dasso, National Institutes of Health, Bethesda, MD) at BamHI and EcoRI, replacing the EGFP sequence to generate a bacterial expression construct for GST-mCherry-NLS (pDL94). GST-mCherry-NLS protein was purified similarly to GST-GFP-NLS (Levy and Heald, 2010). Karsten Weis (ETH Zurich, Zurich, Switzerland) provided the bacterial expression constructs for Npm2 (pKW372), Npm-core (pKW373), and His-IBB (pKW312, IBB = amino acids 1–65 of hSRP1α), and these proteins were expressed and purified as previously described (Görlich et al., 1994; Weis et al., 1996). The H2A/H2B histone dimers and H3/H4 histone tetramers were purified from chicken erythrocytes. Recombinant *X. laevis* importin α2 was purified from pKW769 (a gift from Karsten Weis) as previously described (Görlich et al., 1994). Recombinant human nucleolin was obtained from ProSpec (#PRO-1508). Recombinant human proliferating cell nuclear antigen was obtained from LifeSpan BioSciences (LS-G26336-100).

mRNA

Importin α2-E mRNA was synthesized as previously described (Levy and Heald, 2010). The following mutations were introduced into the Npm2 bacterial expression construct (pKW372) by Gibson assembly cloning: mutant 1, $_{123}$YSWAEEED$_{130}$ → $_{123}$AAAAAAAA$_{130}$ (Warren et al., 2017); mutant 2, Y123A;W125A (Warren et al., 2017); and mutant 3, $_{36}$DDEE$_{39}$ → $_{36}$QQQQ$_{39}$ (Salvany et al., 2004). The wild-type and mutant Npm2 sequences were cloned by PCR into pCS2+ at EcoRI/XhoI. The plasmids were linearized with NotI, and mRNA was expressed from the SP6 promoter using the mMessage mMachine kit (Ambion) and isolated in water.

Immunofluorescence and microscopy

Immunofluorescence was performed on nuclei isolated from egg or embryo extracts as previously described (Edens and Levy, 2014, 2016). Briefly, extract containing nuclei was mixed with 20 volumes of fix buffer (ELB, 15% glycerol, and 2.6% paraformaldehyde), rotated for 15 min at room temperature, layered over 5 ml cushion buffer (XB, 200 mM sucrose, and 25% glycerol), and spun onto 12-mm circular coverslips at 1,000 *g* for 15 min at 16°C. Nuclei on coverslips were postfixed in cold methanol for 5 min and rehydrated in PBS–0.1% NP-40. Coverslips were blocked with PBS–3% BSA overnight at 4°C, incubated at room temperature for 1 h each with primary and secondary antibodies diluted in PBS–3% BSA, and stained with 10 µg/ml Hoechst for 5 min. After each incubation, six washes were performed with PBS–0.1% NP-40. Coverslips were mounted in Vectashield mounting medium (catalog no. H-1000; Vector Laboratories) onto glass slides and sealed with nail polish. Primary antibodies included mAb414 (902901, mouse, 1:1,000; BioLegend) that recognizes NPC FG repeats, histone H2B antibody (07-371, rabbit, 1:100; Millipore), *X. laevis* Npm2 antibody (a gift from David Shechter; rabbit, 1:1,000), and acetyl-histone H3 antibody (06-599, rabbit, 1:500; Millipore) that recognizes N-terminal H3 acetylation. Secondary antibodies included 1:1,000 dilutions of Alexa Fluor 488 and 568 anti-mouse IgG (A-11001 and A-11004; Molecular Probes) and Alexa Fluor 488 and 568 anti-rabbit IgG (A-11008 and A-11011; Molecular Probes).

Wide-field microscopy was performed using an Olympus BX63 upright wide-field epifluorescence microscope. This system is equipped to perform multimode, time-lapse imaging using an X-Cite 120LED illumination system. Image acquisition was with a high-resolution Hamamatsu ORCA-Flash4.0 digital CMOS camera at room temperature. Olympus objectives included the PLanApoN 2× (NA 0.08, air), UPLanFLN 20× (NA 0.5, air), and UPLanSApo 40× (NA 1.25, silicon oil). X-Y and Z positions were controlled by a fully motorized Olympus stage. Acquisition and automation were controlled by Olympus cellSens imaging software, and image analysis was performed using Metamorph software (Molecular Devices). Images for measuring fluorescence intensity were acquired using the same exposure times. Total fluorescence intensity and CS nuclear area were measured from original thresholded images using Metamorph software. For nuclear size measurements, live nuclei in droplets were visualized with GFP-NLS or mCherry-NLS, while fixed nuclei spun onto coverslips were visualized with mAb414. Nuclear and droplet volumes were extrapolated from CS area measurements, as previous data showed that CS area accurately predicts total nuclear surface area and volume as measured from confocal z-stacks (Edens and Levy, 2014; Jevtić and Levy, 2015; Levy and Heald, 2010; Vuković et al., 2016). For publication, images were cropped using ImageJ but were otherwise unaltered.

Confocal imaging was performed on a spinning-disk confocal microscope based on an Olympus IX81 microscope stand equipped with a five-line LMM5 laser launch (Spectral Applied Research) and Yokogawa CSU-X1 spinning-disk head. Confocal images were acquired with an EM-CCD camera (ImagEM; Hamamatsu). Z-axis focus was controlled using a piezo Pi-Foc (Physik Instrumentes), and multiposition imaging was achieved using a motorized Ludl stage. Olympus objective PlanApo 100× (NA 1.4, oil) was used. Image acquisition and all system components were controlled using Metamorph software. To measure chromatin relative area, confocal CS images of Hoechst-stained nuclei were acquired. Using MetaMorph, thresholding was applied to obtain the area of only the Hoechst-stained chromatin, and then less stringent thresholding was applied to obtain total nuclear CS area. Finally, chromatin relative area was calculated by dividing the area occupied by Hoechst-staining chromatin by total nuclear area. To quantify the distribution of chromatin within the nucleus, we acquired two Hoechst intensity line scans through the middle of each nucleus using ImageJ. We reasoned that intensity values along these lines would vary greatly for a heterogeneous chromatin distribution and show less variability for a more uniform chromatin distribution. To measure this variability, the SD of all intensity values along each line was determined and normalized to the average intensity to obtain a value we term the chromatin heterogeneity index. Larger values correspond to a more heterogeneous chromatin distribution.

Western blots

Protein samples (e.g., extract, cytosol, fractionated extract, and purified Npm2) were supplemented with SDS-PAGE loading buffer (0.05% Bromophenol blue, 0.1 M DTT, 10% glycerol, 2% SDS, and 0.05 M Tris-Cl, pH 6.8) and boiled for 10 min. Proteins were separated on 10% or 12% SDS-PAGE gels and transferred to Immobilon-FL polyvinylidene difluoride membrane (catalog no. IPFL00010; Millipore) using a tank blotting apparatus (Bio-Rad Laboratories). The membrane was blocked in Odyssey Blocking Buffer (catalog no. 927-40000; LI-COR Biosciences) for 60 min at room temperature and probed with primary antibodies diluted in 1:3 Odyssey Blocking Buffer/PBS plus 0.1% Tween 20 (PBST) overnight at 4°C. Three 10-min washes were performed in PBST. Membranes were then probed with secondary antibodies diluted in Odyssey Blocking Buffer supplemented with 0.01% SDS and 0.1% Tween 20 for 60 min at room temperature. Three 10-min washes were performed in PBST. Membranes were then rinsed in water and scanned on an Odyssey CLx instrument (LI-COR Biosciences). Band intensities were quantified using Odyssey software (ImageStudio). Primary antibodies included *X. laevis* Npm2 antibody (a gift from David Shechter; rabbit, 1:1,000) and β-tubulin antibody (catalog no. sc-58884, mouse, 1:100; Santa Cruz Biotechnology). Secondary antibodies used at 1:20,000 were IRDye 800CW anti-rabbit (926-32211; LI-COR Biosciences) and IRDye 680RD anti-mouse (925-68070; LI-COR Biosciences).

MNase digestion assay

Stage 10 embryo extract was diluted 10-fold with ELB, and nuclei were pelleted by centrifugation at 3,000 *g* for 5 min. Nuclei were suspended in MNase buffer (50 mM Tris-HCl and 5 mM $CaCl_2$, pH 7.9) containing 5 U/µl MNase and incubated for different periods of time at room temperature. Reactions were stopped with 30 mM EDTA and treated with 0.2 mg/ml Proteinase K and 0.5% SDS at 50°C for 30 min. DNA was extracted with 25:24:1 phenol/chloroform/isoamyl alcohol (catalog no. p3803; Sigma) and precipitated with 0.3 M NaOAc and 66% ethanol at −20°C overnight. DNA was isolated by centrifugation, washed with 70% ethanol, and resuspended in TE buffer. DNA was run on 2% agarose gels in 1× TAE buffer along with the Fast DNA Ladder (catalog no. N3238; NEB) and visualized with ethidium bromide. To quantify the average nucleosome number per fragment, the intensity (I) of each band corresponding to one to six nucleosomes was quantified, and the following equation was used to calculate average nucleosome number:

$$\frac{\begin{array}{c}\mathrm{I}\ (\text{hexa}-)\times 6+\mathrm{I}\ (\text{penta}-)\times 5+\mathrm{I}\ (\text{tetra}-)\times\\ 4+\mathrm{I}\ (\text{tri}-)\times 3+\mathrm{I}\ (\text{di}-)\times 2+\mathrm{I}\ (\text{mono}-)\times 1\end{array}}{\begin{array}{c}\mathrm{I}\ (\text{hexa}-)+\mathrm{I}\ (\text{penta}-)+\mathrm{I}\ (\text{tetra}-)+\\ \mathrm{I}\ (\text{tri}-)+\mathrm{I}\ (\text{di}-)+\mathrm{I}\ (\text{mono}-)\end{array}}.$$

Statistical analysis

Averaging and statistical analysis were performed for independently repeated experiments. Where indicated, nuclear size and intensity measurements were normalized to controls. Two-tailed Student's t tests assuming equal variances were performed with Minitab 18 or Prism 6 to evaluate statistical significance. For each immunofluorescence coverslip, generally >100 nuclei were quantified. The P values, number of independent experiments, number of nuclei quantified, and error bars are denoted in the figure legends.

Online supplemental material

Fig. S1 presents further characterization of the contribution of cytoplasmic volume and composition to nuclear size scaling. Fig. S2 shows identification of Npm2 as a nuclear-sizing factor by fractionation. Fig. S3 presents testing of components limiting for in vitro nuclear growth. Fig. S4 shows testing of other cargos, chromatin topology measurements, and transcription-independent effects of Npm2 on nuclear size. Video 1 shows nuclear growth in a 1-nl spherical droplet.

Acknowledgments

We thank David Shechter for antibodies and Npm2 mutant advice, Kenneth Gerow (University of Wyoming, Laramie, WY) for help with statistical analysis, Nicolas Blouin and Vikram Chhatre (University of Wyoming, Laramie, WY) for bioinformatics help identifying NLS-containing proteins, Priscilla Phan for egg extract preparation, David Fay for constructive comments on the manuscript, and members of the Levy, Gatlin, and Oakey laboratories for helpful advice and discussions.

This work was supported by the National Institutes of Health/National Institute of General Medical Sciences (grants R01GM113028 and P20GM103432), the American Cancer Society (grant RSG-15-035-01-DDC), and the National Science Foundation (Faculty CAREER program BBBE 1254608).

The authors declare no competing financial interests.

Author contributions: Conceptualization, P. Chen, J. Oakey, J.C. Gatlin, and D.L. Levy; Methodology, K.M. Nelson and J. Oakey designed and fabricated the microfluidic devices; Investigation, P. Chen performed all experiments and M. Tomschik performed the fractionations; Writing – Original Draft, P. Chen and D.L. Levy; Writing – Review & Editing, P. Chen, M. Tomschik, K.M. Nelson, J. Oakey, J.C. Gatlin, and D.L. Levy; Funding Acquisition, J. Oakey, J.C. Gatlin, and D.L. Levy.

Submitted: 19 February 2019
Revised: 8 July 2019
Accepted: 6 September 2019

References

Amodeo, A.A., D. Jukam, A.F. Straight, and J.M. Skotheim. 2015. Histone titration against the genome sets the DNA-to-cytoplasm threshold for the Xenopus midblastula transition. *Proc. Natl. Acad. Sci. USA.* 112: E1086–E1095. https://doi.org/10.1073/pnas.1413990112

Aranda-Anzaldo, A. 2016. The interphase mammalian chromosome as a structural system based on tensegrity. *J. Theor. Biol.* 393:51–59. https://doi.org/10.1016/j.jtbi.2016.01.005

Baarlink, C., M. Plessner, A. Sherrard, K. Morita, S. Misu, D. Virant, E.M. Kleinschnitz, R. Harniman, D. Alibhai, S. Baumeister, et al. 2017. A transient pool of nuclear F-actin at mitotic exit controls chromatin organization. *Nat. Cell Biol.* 19:1389–1399. https://doi.org/10.1038/ncb3641

Bogdanović, O., S.J. van Heeringen, and G.J. Veenstra. 2012. The epigenome in early vertebrate development. *Genesis.* 50:192–206. https://doi.org/10.1002/dvg.20831

Brownlee, C., and R. Heald. 2019. Importin alpha Partitioning to the Plasma Membrane Regulates Intracellular Scaling. *Cell.* 176:805–815.e8. https://doi.org/10.1016/j.cell.2018.12.001

Burgess, R.J., and Z. Zhang. 2013. Histone chaperones in nucleosome assembly and human disease. *Nat. Struct. Mol. Biol.* 20:14–22. https://doi.org/10.1038/nsmb.2461

Burns, K.H., M.M. Viveiros, Y. Ren, P. Wang, F.J. DeMayo, D.E. Frail, J.J. Eppig, and M.M. Matzuk. 2003. Roles of NPM2 in chromatin and nucleolar organization in oocytes and embryos. *Science.* 300:633–636. https://doi.org/10.1126/science.1081813

Bustin, M., and T. Misteli. 2016. Nongenetic functions of the genome. *Science.* 352:aad6933. https://doi.org/10.1126/science.aad6933

Chalut, K.J., M. Höpfler, F. Lautenschläger, L. Boyde, C.J. Chan, A. Ekpenyong, A. Martinez-Arias, and J. Guck. 2012. Chromatin decondensation and nuclear softening accompany Nanog downregulation in embryonic stem cells. *Biophys. J.* 103:2060–2070. https://doi.org/10.1016/j.bpj.2012.10.015

Chen, P., and D.L. Levy. 2018. Nucleus Assembly and Import in *Xenopus laevis* Egg Extract. *Cold Spring Harb. Protoc.* 2018:pdb.prot097196. https://doi.org/10.1101/pdb.prot097196

Conklin, E. 1912. Cell size and nuclear size. *J. Exp. Embryol.* 12:1–98.

Cox, L.S. 1992. DNA replication in cell-free extracts from Xenopus eggs is prevented by disrupting nuclear envelope function. *J. Cell Sci.* 101:43–53.

Duffy, D.C., J.C. McDonald, O.J. Schueller, and G.M. Whitesides. 1998. Rapid Prototyping of Microfluidic Systems in Poly(dimethylsiloxane). *Anal. Chem.* 70:4974–4984. https://doi.org/10.1021/ac980656z

Duncan, T., and T.T. Su. 2004. Embryogenesis: coordinating cell division with gastrulation. *Curr. Biol.* 14:R305–R307. https://doi.org/10.1016/j.cub.2004.03.050

Earnshaw, W.C., B.M. Honda, R.A. Laskey, and J.O. Thomas. 1980. Assembly of nucleosomes: the reaction involving X. laevis nucleoplasmin. *Cell.* 21: 373–383. https://doi.org/10.1016/0092-8674(80)90474-2

Edens, L.J., and D.L. Levy. 2014. cPKC regulates interphase nuclear size during Xenopus development. *J. Cell Biol.* 206:473–483. https://doi.org/10.1083/jcb.201406004

Edens, L.J., and D.L. Levy. 2016. A Cell-Free Assay Using Xenopus laevis Embryo Extracts to Study Mechanisms of Nuclear Size Regulation. *J. Vis. Exp.* (114). https://doi.org/10.3791/54173

Edens, L.J., M.R. Dilsaver, and D.L. Levy. 2017. PKC-mediated phosphorylation of nuclear lamins at a single serine residue regulates interphase nuclear size in *Xenopus* and mammalian cells. *Mol. Biol. Cell.* 28: 1389–1399. https://doi.org/10.1091/mbc.e16-11-0786

Eng, J.K., A.L. McCormack, and J.R. Yates. 1994. An approach to correlate tandem mass spectral data of peptides with amino acid sequences in a protein database. *J. Am. Soc. Mass Spectrom.* 5:976–989. https://doi.org/10.1016/1044-0305(94)80016-2

Frehlick, L.J., J.M. Eirín-López, and J. Ausió. 2007. New insights into the nucleophosmin/nucleoplasmin family of nuclear chaperones. *BioEssays.* 29:49–59. https://doi.org/10.1002/bies.20512

Goehring, N.W., and A.A. Hyman. 2012. Organelle growth control through limiting pools of cytoplasmic components. *Curr. Biol.* 22:R330–R339. https://doi.org/10.1016/j.cub.2012.03.046

Good, M.C., and R. Heald. 2018. Preparation of Cellular Extracts from Xenopus Eggs and Embryos. *Cold Spring Harb. Protoc.* 2018:pdb.prot097055. https://doi.org/10.1101/pdb.prot097055

Görlich, D., S. Prehn, R.A. Laskey, and E. Hartmann. 1994. Isolation of a protein that is essential for the first step of nuclear protein import. *Cell.* 79:767–778. https://doi.org/10.1016/0092-8674(94)90067-1

Grisendi, S., C. Mecucci, B. Falini, and P.P. Pandolfi. 2006. Nucleophosmin and cancer. *Nat. Rev. Cancer.* 6:493–505. https://doi.org/10.1038/nrc1885

Gurard-Levin, Z.A., J.P. Quivy, and G. Almouzni. 2014. Histone chaperones: assisting histone traffic and nucleosome dynamics. *Annu. Rev. Biochem.* 83:487–517. https://doi.org/10.1146/annurev-biochem-060713-035536

Gurdon, J.B. 1976. Injected nuclei in frog oocytes: fate, enlargement, and chromatin dispersal. *J. Embryol. Exp. Morphol.* 36:523–540.

Hara, Y., and C.A. Merten. 2015. Dynein-Based Accumulation of Membranes Regulates Nuclear Expansion in Xenopus laevis Egg Extracts. *Dev. Cell.* 33:562–575. https://doi.org/10.1016/j.devcel.2015.04.016

Hara, Y., M. Iwabuchi, K. Ohsumi, and A. Kimura. 2013. Intranuclear DNA density affects chromosome condensation in metazoans. *Mol. Biol. Cell.* 24:2442–2453. https://doi.org/10.1091/mbc.e13-01-0043

Hazel, J.W., and J.C. Gatlin. 2018. Isolation and Demembranation of Xenopus Sperm Nuclei. *Cold Spring Harb. Protoc.* 2018:pdb.prot099044. https://doi.org/10.1101/pdb.prot099044

Hazel, J., K. Krutkramelis, P. Mooney, M. Tomschik, K. Gerow, J. Oakey, and J.C. Gatlin. 2013. Changes in cytoplasmic volume are sufficient to drive spindle scaling. *Science.* 342:853–856. https://doi.org/10.1126/science.1243110

Hontelez, S., I. van Kruijsbergen, G. Georgiou, S.J. van Heeringen, O. Bogdanovic, R. Lister, and G.J.C. Veenstra. 2015. Embryonic transcription is controlled by maternally defined chromatin state. *Nat. Commun.* 6: 10148. https://doi.org/10.1038/ncomms10148

Ingber, D.E. 2003. Tensegrity I. Cell structure and hierarchical systems biology. *J. Cell Sci.* 116:1157–1173. https://doi.org/10.1242/jcs.00359

Inoue, A., and Y. Zhang. 2014. Nucleosome assembly is required for nuclear pore complex assembly in mouse zygotes. *Nat. Struct. Mol. Biol.* 21: 609–616. https://doi.org/10.1038/nsmb.2839

Jevtić, P., and D.L. Levy. 2014. Mechanisms of nuclear size regulation in model systems and cancer. *Adv. Exp. Med. Biol.* 773:537–569. https://doi.org/10.1007/978-1-4899-8032-8_25

Jevtić, P., and D.L. Levy. 2015. Nuclear size scaling during Xenopus early development contributes to midblastula transition timing. *Curr. Biol.* 25: 45–52. https://doi.org/10.1016/j.cub.2014.10.051

Jevtić, P., L.J. Edens, X. Li, T. Nguyen, P. Chen, and D.L. Levy. 2015. Concentration-dependent Effects of Nuclear Lamins on Nuclear Size in Xenopus and Mammalian Cells. *J. Biol. Chem.* 290:27557–27571. https://doi.org/10.1074/jbc.M115.673798

Keck, K.M., and L.F. Pemberton. 2013. Histone chaperones link histone nuclear import and chromatin assembly. *Biochim. Biophys. Acta.* 1819: 277–289. https://doi.org/10.1016/j.bbagrm.2011.09.007

Kim, Y.H., M.E. Han, and S.O. Oh. 2017. The molecular mechanism for nuclear transport and its application. *Anat. Cell Biol.* 50:77–85. https://doi.org/10.5115/acb.2017.50.2.77

Kirby, T.J., and J. Lammerding. 2018. Emerging views of the nucleus as a cellular mechanosensor. *Nat. Cell Biol.* 20:373–381. https://doi.org/10.1038/s41556-018-0038-y

Kırlı, K., S. Karaca, H.J. Dehne, M. Samwer, K.T. Pan, C. Lenz, H. Urlaub, and D. Görlich. 2015. A deep proteomics perspective on CRM1-mediated nuclear export and nucleocytoplasmic partitioning. *eLife.* 4:e11466. https://doi.org/10.7554/eLife.11466

Kopito, R.B., and M. Elbaum. 2007. Reversibility in nucleocytoplasmic transport. *Proc. Natl. Acad. Sci. USA.* 104:12743–12748. https://doi.org/10.1073/pnas.0702690104

Lemaitre, J.M., G. Géraud, and M. Méchali. 1998. Dynamics of the genome during early Xenopus laevis development: karyomeres as independent units of replication. *J. Cell Biol.* 142:1159–1166. https://doi.org/10.1083/jcb.142.5.1159

Levy, D.L., and R. Heald. 2010. Nuclear size is regulated by importin α and Ntf2 in Xenopus. *Cell.* 143:288–298. https://doi.org/10.1016/j.cell.2010.09.012

Mukherjee, R.N., P. Chen, and D.L. Levy. 2016. Recent advances in understanding nuclear size and shape. *Nucleus.* 7:167–186. https://doi.org/10.1080/19491034.2016.1162933

Murakami, M.S., S.A. Moody, I.O. Daar, and D.K. Morrison. 2004. Morphogenesis during Xenopus gastrulation requires Wee1-mediated inhibition of cell proliferation. *Development.* 131:571–580. https://doi.org/10.1242/dev.00971

Neumann, F.R., and P. Nurse. 2007. Nuclear size control in fission yeast. *J. Cell Biol.* 179:593–600. https://doi.org/10.1083/jcb.200708054

Newport, J., and M. Kirschner. 1982. A major developmental transition in early Xenopus embryos: I. characterization and timing of cellular changes at the midblastula stage. *Cell.* 30:675–686. https://doi.org/10.1016/0092-8674(82)90272-0

Newport, J.W., K.L. Wilson, and W.G. Dunphy. 1990. A lamin-independent pathway for nuclear envelope assembly. *J. Cell Biol.* 111:2247–2259. https://doi.org/10.1083/jcb.111.6.2247

Nguyen, T., N. Pappireddi, and M. Wühr. 2019. Proteomics of nucleocytoplasmic partitioning. *Curr. Opin. Chem. Biol.* 48:55–63. https://doi.org/10.1016/j.cbpa.2018.10.027

Nieuwkoop, P.D., and J. Faber. 1967. *Normal Table of Xenopus laevis (Daudin).* North-Holland Publishing Company, Amsterdam.

Oakey, J., and J.C. Gatlin. 2018. Microfluidic Encapsulation of Demembranated Sperm Nuclei in *Xenopus* Egg Extracts. *Cold Spring Harb. Protoc.* 2018:pdb.prot102913. https://doi.org/10.1101/pdb.prot102913

Onikubo, T., and D. Shechter. 2016. Chaperone-mediated chromatin assembly and transcriptional regulation in Xenopus laevis. *Int. J. Dev. Biol.* 60: 271–276. https://doi.org/10.1387/ijdb.130188ds

Onikubo, T., J.J. Nicklay, L. Xing, C. Warren, B. Anson, W.L. Wang, E.S. Burgos, S.E. Ruff, J. Shabanowitz, R.H. Cheng, et al. 2015. Developmentally Regulated Post-translational Modification of Nucleoplasmin Controls Histone Sequestration and Deposition. *Cell Reports.* 10: 1735–1748. https://doi.org/10.1016/j.celrep.2015.02.038

Peng, J., and S.P. Gygi. 2001. Proteomics: the move to mixtures. *J. Mass Spectrom.* 36:1083–1091. https://doi.org/10.1002/jms.229

Peshkin, L., M. Wühr, E. Pearl, W. Haas, R.M. Freeman Jr., J.C. Gerhart, A.M. Klein, M. Horb, S.P. Gygi, and M.W. Kirschner. 2015. On the Relationship of Protein and mRNA Dynamics in Vertebrate Embryonic Development. *Dev. Cell.* 35:383–394. https://doi.org/10.1016/j.devcel.2015.10.010

Philpott, A., G.H. Leno, and R.A. Laskey. 1991. Sperm decondensation in Xenopus egg cytoplasm is mediated by nucleoplasmin. *Cell.* 65:569–578. https://doi.org/10.1016/0092-8674(91)90089-H

Platonova, O., I.V. Akey, J.F. Head, and C.W. Akey. 2011. Crystal structure and function of human nucleoplasmin (npm2): a histone chaperone in oocytes and embryos. *Biochemistry.* 50:8078–8089. https://doi.org/10.1021/bi2006652

Salvany, L., M. Chiva, C. Arnan, J. Ausió, J.A. Subirana, and N. Saperas. 2004. Mutation of the small acidic tract A1 drastically reduces nucleoplasmin activity. *FEBS Lett.* 576:353–357. https://doi.org/10.1016/j.febslet.2004.07.095

Shevchenko, A., M. Wilm, O. Vorm, and M. Mann. 1996. Mass spectrometric sequencing of proteins silver-stained polyacrylamide gels. *Anal. Chem.* 68:850–858. https://doi.org/10.1021/ac950914h

Shimamoto, Y., S. Tamura, H. Masumoto, and K. Maeshima. 2017. Nucleosome-nucleosome interactions via histone tails and linker DNA regulate nuclear rigidity. *Mol. Biol. Cell.* 28:1580–1589. https://doi.org/10.1091/mbc.e16-11-0783

Sive, H.L., R.M. Grainger, and R.M. Harland. 2000. Early Development of *Xenopus laevis*: A Laboratory Manual. Cold Spring Harbor Laboratory Press, Cold Spring Harbor, NY. 338 pp.

Stephens, A.D., E.J. Banigan, S.A. Adam, R.D. Goldman, and J.F. Marko. 2017. Chromatin and lamin A determine two different mechanical response regimes of the cell nucleus. *Mol. Biol. Cell.* 28:1984–1996. https://doi.org/10.1091/mbc.e16-09-0653

Stephens, A.D., P.Z. Liu, E.J. Banigan, L.M. Almassalha, V. Backman, S.A. Adam, R.D. Goldman, and J.F. Marko. 2018. Chromatin histone modifications and rigidity affect nuclear morphology independent of lamins. *Mol. Biol. Cell.* 29:220–233. https://doi.org/10.1091/mbc.E17-06-0410

Sun, L., M.M. Bertke, M.M. Champion, G. Zhu, P.W. Huber, and N.J. Dovichi. 2014. Quantitative proteomics of Xenopus laevis embryos: expression kinetics of nearly 4000 proteins during early development. *Sci. Rep.* 4: 4365. https://doi.org/10.1038/srep04365

Vuković, L.D., P. Jevtić, Z. Zhang, B.A. Stohr, and D.L. Levy. 2016. Nuclear size is sensitive to NTF2 protein levels in a manner dependent on Ran binding. *J. Cell Sci.* 129:1115–1127. https://doi.org/10.1242/jcs.181263

Warren, C., T. Matsui, J.M. Karp, T. Onikubo, S. Cahill, M. Brenowitz, D. Cowburn, M. Girvin, and D. Shechter. 2017. Dynamic intramolecular regulation of the histone chaperone nucleoplasmin controls histone binding and release. *Nat. Commun.* 8:2215. https://doi.org/10.1038/s41467-017-02308-3

Webster, M., K.L. Witkin, and O. Cohen-Fix. 2009. Sizing up the nucleus: nuclear shape, size and nuclear-envelope assembly. *J. Cell Sci.* 122: 1477–1486. https://doi.org/10.1242/jcs.037333

Weis, K., U. Ryder, and A.I. Lamond. 1996. The conserved amino-terminal domain of hSRP1 alpha is essential for nuclear protein import. *EMBO J.* 15:1818–1825. https://doi.org/10.1002/j.1460-2075.1996.tb00531.x

Wilbur, J.D., and R. Heald. 2013. Mitotic spindle scaling during Xenopus development by kif2a and importin α. *eLife.* 2:e00290. https://doi.org/10.7554/eLife.00290

Wilson, E.B. 1925. The karyoplasmic ratio. *In The Cell in Development and Heredity.* The Macmillan Company, New York. 727–733.

Wühr, M., T. Güttler, L. Peshkin, G.C. McAlister, M. Sonnett, K. Ishihara, A.C. Groen, M. Presler, B.K. Erickson, T.J. Mitchison, et al. 2015. The Nuclear Proteome of a Vertebrate. *Curr. Biol.* 25:2663–2671. https://doi.org/10.1016/j.cub.2015.08.047

Zidovska, A., D.A. Weitz, and T.J. Mitchison. 2013. Micron-scale coherence in interphase chromatin dynamics. *Proc. Natl. Acad. Sci. USA.* 110: 15555–15560. https://doi.org/10.1073/pnas.1220313110

Zierhut, C., C. Jenness, H. Kimura, and H. Funabiki. 2014. Nucleosomal regulation of chromatin composition and nuclear assembly revealed by histone depletion. *Nat. Struct. Mol. Biol.* 21:617–625. https://doi.org/10.1038/nsmb.2845

Zink, D., A.H. Fischer, and J.A. Nickerson. 2004. Nuclear structure in cancer cells. *Nat. Rev. Cancer.* 4:677–687. https://doi.org/10.1038/nrc1430